Northumbria Research Link

Northumbria
University
NEWCASTLE

Sol-Carolina Costa
Department of Mechanical and Construction,
Northumbria University,
Newcastle upon Tyne NE1 8ST, UK
e-mail: carolina.costa@northumbria.ac.uk

Khamid Mahkamov
Department of Mechanical and Construction,
Northumbria University,
Newcastle upon Tyne NE1 8ST, UK
e-mail: khamid.mahkamov@northumbria.ac.uk

Murat Kenisarin
Department of Mechanical and Construction,
Northumbria University,
Newcastle upon Tyne NE1 8ST, UK
e-mail: murat.kenisarin@northumbria.ac.uk

Mohammad Ismail
Department of Mechanical and Construction,
Northumbria University,
Newcastle upon Tyne NE1 8ST, UK
e-mail: mohammad.ismail@northumbria.ac.uk

Kevin Lynn
Aavid Thermacore Europe Ltd,
Ashington, Northumberland NE63 8QW, UK
e-mail: kevin.lynn@boydcorp.com

Elvedin Halimic
Aavid Thermacore Europe Ltd,
Ashington, Northumberland NE63 8QW, UK
e-mail: Elvedin.Halimic@boydcorp.com

David Mullen
Aavid Thermacore Europe Ltd,
Ashington, Northumberland NE63 8QW, UK
e-mail: David.Mullen@boydcorp.com

Solar Salt Latent Heat Thermal Storage for a Small Solar Organic Rankine Cycle Plant

The design of the latent heat thermal storage system (LHTESS) was developed with a thermal capacity of about 100 kW h as a part of small solar plant based on the organic Rankine cycle (ORC). The phase change material (PCM) used is solar salt with the melting/solidification temperature of about 220 °C. Thermophysical properties of the PCM were measured, including its phase transition temperature, heat of fusion, specific heat, and thermal conductivity. The design of the thermal storage was finalized by means of the 3D computational fluid dynamics analysis. The thermal storage system is modular, and the thermal energy is delivered with the use of thermal oil, heated by Fresnel mirrors. The heat is transferred into and from the PCM in the casing using bidirectional heat pipes, filled with water. A set of metallic screens are installed in the box with the pitch of 8–10 mm to enhance the heat transfer from heat pipes to the PCM and vice-versa during the charging and discharging processes, which take about 4 h. This work presents a numerical study on the use of metallic fins without thermal bonding as a heat transfer enhancement method for the solar salt LHTESS. The results show that the absence of the thermal bonding between fins and heat pipes (there was a gap of 0.5 mm between them) did not result in a significant reduction of charging or discharging periods. As expected, aluminum fins provide better performance in comparison with steel ones due to the difference in the material conductivity. The main advantage observed for the case of using aluminum fins was the lower temperature gradient across the LHTESS. [DOI: 10.1115/1.4044557]

Keywords: alternative energy sources, energy conversion/systems, energy storage systems, energy systems analysis, heat energy generation/storage/transfer, phase change material, solar power plant

1 Introduction

Thermal energy storage is of paramount importance in solar thermal energy conversion plants. Considerable attention has been paid to this problem in high-temperature solar energy plants. Several large-scale high-temperature plants for demonstrational purposes were built across the world and used to investigate more thoroughly thermal storage issues in terms of design and materials selection. The melting and solidification processes of phase change materials (PCMs) have been investigated mainly in simplified geometries, such as cylinders, for different materials. Sasaguchi and Viskanta [1] investigated experimentally two cylindrical heat exchangers using the low-temperature PCM. Aceves-Saborio et al. [2] analyzed the efficiency of a number of latent heat storage systems using different PCMs. Pinelli and Piva [3] investigated numerically the effect of natural convection in the phase change processes in a cylindrical cavity. Archibold et al. [4] investigated numerically and experimentally the heat transfer during the melting process of a high-temperature PCM contained in a porcelain crucible. Studniorz et al. [5] analyzed the application of a latent heat storage system using PCM for existing off-grid telecommunication base stations. Nnaemeka and Bibeau [6] experimentally investigated the effect of tubes with PCM placed inside a fuel tank to avoid the gelling and plugging of fuel filters and piping during a winter period.

The originality of this work is in the design study of LHTESS which is used as a part of micro solar power plant, based on the 2-kWel organic Rankine cycle (ORC) turbine, operating at temperature levels between 220 and 230 °C. One of the tasks was the selection of the most appropriate type of PCM to be used in the thermal storage system. Several design configurations of LHTESS with different internal metallic fin arrays without thermal bonding were investigated to select the rational design, which provides the required thermal energy charging and discharging rate levels to ensure extension of the operational period of the ORC turbine.

2 Selection of the Phase Change Material Through the Evaluation of Thermophysical Properties

In order to provide the optimal operation of the small ORC plant for its selected configuration and materials used, the operational temperature range of the LHTESS was chosen to be between 200 and 230 °C. Within this temperature interval, there are several appropriate PCMs and some of them are listed in Table 1.

Among materials, listed in Table 1, solar salt (60 wt% $NaNO_3$ + 40 wt% KNO_3) and the equimolar eutectic blend (46.7 wt% $NaNO_3$ + 40 wt% KNO_3) are those which were extensively investigated [7–11]. Solar salt is widely used as a heat transfer fluid (HTF) in various industry branches at temperatures up to 550–600 °C. The eutectic compositions of sodium nitrite and sodium hydroxide can

Contributed by the Advanced Energy Systems Division of ASME for publication in the Journal of Energy Resources Technology. Manuscript received March 6, 2019; final manuscript received June 20, 2019; published online September 3, 2019. Assoc. Editor: Samer F. Ahmed.

Table 1 Properties of the perspective PCMs [7–9]

Phase change material	T_m (°C)	T_s (°C)	H_m (J/g)
60 wt% $NaNO_3$ + 40 wt% KNO_3	221	221	96
46.7 wt% $NaNO_3$ + 40 wt% KNO_3	221	221	100
87.3 wt% $NaNO_2$ + 12.7 wt% NaOH	232	232	252
39 wt% $NaNO_2$ + 61 wt% NaOH	237	227	294
Myo-inositol	224	192	260
Tin	232	232	60

also be considered as very strong candidate materials for the project's purpose. However, such compositions require the detailed investigation of their thermophysical properties as well as thermal stability and corrosion effect on construction materials, including metals and alloys. The high heat of fusion makes sugar alcohol myo--inositol an attractive alternative, but it is relatively expensive and has the significant hysteresis equal to 30–40 °C at the temperature of phase change [9]. The latter considerably decreases the thermal efficiency of the ORC turbine. Tin and its alloys can only be used as a PCM in special cases, in which the weight and cost are not of significance for consumers. Thus, solar salt and equimolar eutectic composition are preferred for designing the plant's LHTESS.

For the present project, solar salt was selected as the PCM due to its high stability and availability on the market at relatively low price (less than $1000 per ton). A sample of solar salt was supplied by a company as H220 material with the melting point of 220 °C and heat of fusion equal to 96.6 kJ/kg. The melting temperature, heat of fusion, and heat capacity were determined in the present work using the differential scanning calorimeter (DSC) technique. Solar salt was melted in a steel container in a muffle oven and its conductivity coefficient was measured at the room temperature with a KD2 Pro thermal conductivity analyzer.

The typical DSC curves are shown in Fig. 1. Four measurements produced the average value of the melting point at 218.4 °C and heat of fusion equal to 94.3 J/g. The obtained values are very close to 220 °C and 96.6 J/g, reported by the supplier, and to 220.8 °C and 95.6 J/g, measured by Zhai et al. [7]. The values of heat fusion produced in the present work are significantly lower than that reported in Ref. [13]—118 J/g—and in Ref. [14]—142.3 J/g.

The measured temperature dependence of the specific heat is presented in Fig. 2. The curve of specific heat is practically coincident with data of Iverson et al. [15]. As seen in Fig. 2, the average specific heat of solid state near the solidus temperature is 1.74 kJ/(kg K). This value is 1.5 kJ/(kg K) for the liquid state and remains practically constant at the temperature range up to 350 °C. The specific heat capacity for the melting range, used in further calculation, was determined by the average value of the solid and liquid specific heat

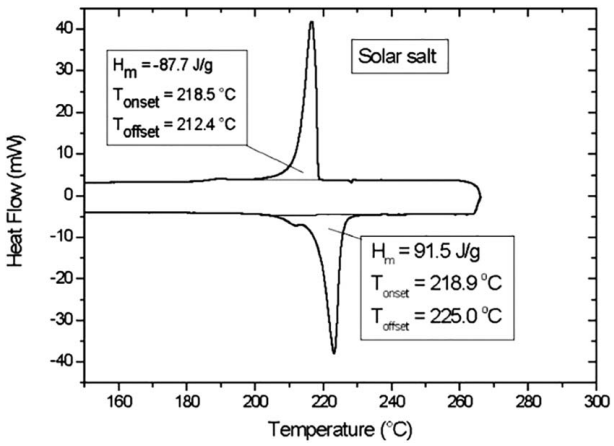

Fig. 1 The typical DSC analysis of pure solar salt (H220, 60 wt% $NaNO_3$ + 40 wt% KNO_3) [12]

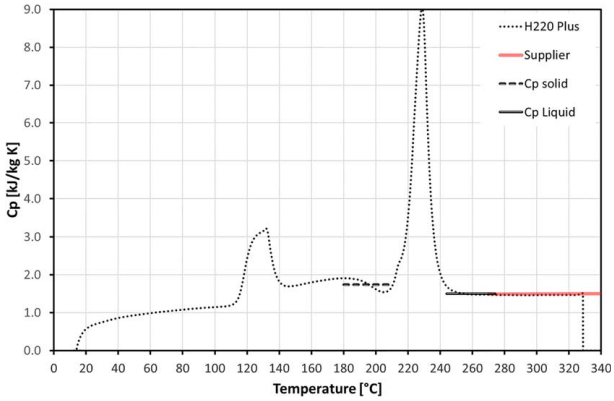

Fig. 2 The specific heat of solar salt (H220, 60 wt% $NaNO_3$ + 40 wt% KNO_3)

Table 2 Solar salt physical properties

Property	Formula	Units	References
$T_{solidus}$	218	°C	[12]
$T_{liquidus}$	230	°C	[12]
H_m	94.3	kJ/kg	[12]
ρ_l	$2106 - 0.680T$ (°C)	kg/m^3	[1]
c_{pl}	1620	J/kg °C	[12]
k_l	$0.380 + 3.452 \times 10^{-4}T$ (°C)	W/m °C	[1]
μ_l	$1/(-0.263 + 0.0020T$ (°C))	cP	[17,18]

capacity as 1.62 kJ/(kg K). This value is very close to 1.55 kJ/(kg K) of Martin et al. [13] and 1.49 kJ/(kg K) of Pacheco et al. [16].

The measurement of the thermal conductivity and thermal diffusivity of solar salt was performed at the room temperature. The measured thermophysical properties of solar salt are not sufficient to carry out numerical simulations and designing the LHTESS since it was also necessary to collect data from published sources on density, thermal conductivity, and viscosity of the molten salt composition. The collected data to be used in numerical simulations are presented in Table 2. Information on the density and thermal conductivity of molten solar salt was systematized by Bauer et al. [11], who summarized previous measurements by various authors. The results of measurements of viscosity were published only in two works, namely, Refs. [17,18].

3 Latent Heat Thermal Storage System

In the small solar power plant designed [19], the LHTESS is arranged to provide thermal energy at the rate of 25 kW for a duration of 4-h period for the ORC unit to deliver electrical power and heat to a dwelling during the night time occupational period.

In order to store such amount of thermal energy as a latent heat, about 3.8 tons of solar salt are necessary, which corresponds to the volume of LHTESS being about 2 m^3. A modular design concept of the LHTESS is adopted, which allows to make up the whole unit with 6–10 single modules. The modular concept also provides more flexibility in the configuration of the whole LHTESS and control of the operational parameters.

The main disadvantage of solar salt is its low thermal conductivity, which makes it impossible to complete the thermal energy charging and discharging at the required rate. Therefore, it is necessary to deploy methods, which would enhance heat transfer in the LHTESS. The heat transfer enhancement can be achieved by increasing the thermal conductivity of the PCM by means of adding high thermal conductive particles and placing high thermal conductivity inserts into the PCM such as metallic fins or combination of different methods [20,21]. One of the approaches considered in the project was the use of reversible heat pipes in

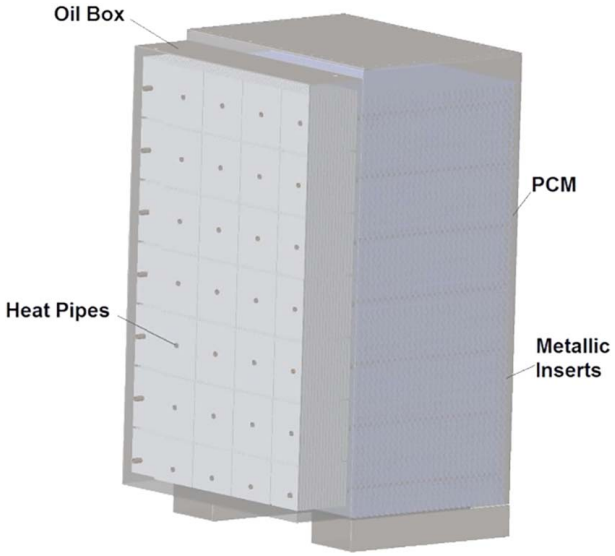

Fig. 3 LHTESS single module

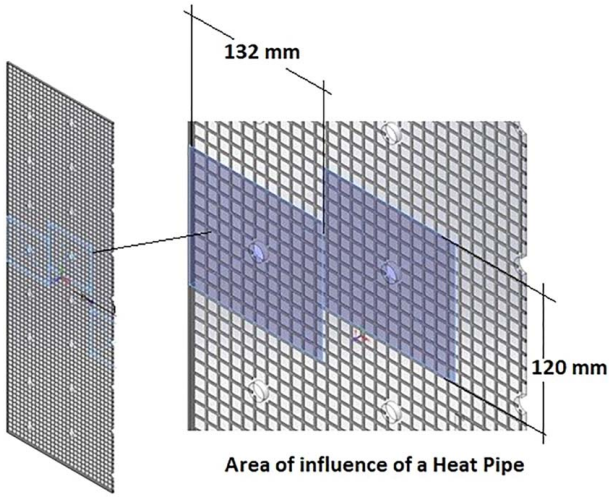

Fig. 4 The vertical cross-cut of the half of fin with a symmetry plane in the module of LHTESS

combination with metallic inserts. Figure 3 shows the general design of the single module of LHTESS.

The module is divided into two main volumes: the first is the oil reservoir with the inlet and outlet for the HTF, which is thermal oil. The HTF flowing from the solar field with the high-temperature passes thermal energy to heat pipes through their evaporation zones and then this heat flux is used to charge the LHTESS. In case of the HTF, temperature decreased below the PCM's temperature; the heat pipes will transport heat in the opposite direction, namely, from the PCM to HTF. In the oil reservoir zone, the heat pipe heat transfer area is increased using metallic fins welded to tubes of heat pipes. Horizontal stainless-steel cartridges run through this section of the storage and house heat pipes.

The vertical metallic inserts are used as fins for enhancing the heat transfer during charging and discharging processes. A set of holes is drilled in these vertical fins to run through stainless cartridges. The heat is transferred from heat pipes to the PCM and vertical fins through the wall of the stainless-steel cartridges. One of the challenges in designing the LHTESS is the selection of the rational configuration of these fins (pitch size; perforated or plane geometry) in order to maximize the thermal capacity and performance with the minimal increase in weight and cost. The heat pipes transfer thermal energy at the maximum rate of 120 W each and the required number of heat pipes should also be defined during the designing process.

In the project, other methods for increasing the thermal conductivity of pure solar salt were also investigated, including the use of expanded graphite and metal foams [12].

4 3D Computational Fluid Dynamics Numerical Modeling of the Latent Heat Thermal Storage System

The aim of the numerical modeling is the selection of the best configuration of metallic inserts and heat pipes inside the storage module in order to achieve the required rate of thermal energy charging and discharging. To reduce the computational time, the numerical modeling uses a simplified representation of the module by its small fraction, located between metallic inserts and which surrounds the single heat pipe and is enclosed by symmetry planes. This region is called the LHTESS cell unit in this work. Another simplification is that the physical phenomena inside heat pipes is not considered at initial stages of investigation, and these are modeled as solid bars with a very high thermal conductivity [22,23] or as a constant heat flux device [24]. In this study, the second approach was implemented.

The physical geometry of a single metallic insert/fin with heat pipes embedded is shown in Fig. 4. The width and height of the frontal selected area per heat pipe are 132 mm and 120 mm, respectively. In this study, the thickness of the metallic inserts is assumed to be 1.5 mm. The pitch between fins is 10 (cases 1–3) and 8 mm (case 4). Two types of inserts were modeled, namely, plane and perforated ones (shown in Fig. 4). Materials of numerically evaluated fins are steel and aluminum. The perforated fins have an open area of 70%, square holes of 10 mm with the pitch of 12 mm and thickness of 1.5 mm. The features of all cases, studied in this project, are shown in Table 3.

In the first two cases, presented in Table 3 (plates), the mass of PCM in the LHTESS module is 515 kg; therefore, the LHTESS will consist of eight modules. In the last two cases, perforated plates were deployed and this increases the mass of PCM to 580 kg, and therefore, there will be seven single modules in the LHTESS.

The commercial software ANSYS FLUENT 18.2 was used for modeling solidification/melting processes in the 3D geometry of the representative computational region of the LHTESS (see Fig. 5). The enthalpy-porosity technique [22–25] is used to model the PCM melting and solidification. In this technique, the mushy zones of PCM are considered as porous media and the porosity of each element in the mushy zone is assumed to be equal to the liquid fraction (LF) of that element. The enthalpy of the material is computed as the sum of the sensible enthalpy, h, and the latent heat, ΔH [26]

$$H = h + \Delta H \tag{1}$$

where

$$h = h_{\text{ref}} + \int_{T_{\text{ref}}}^{T} c_p dT \tag{2}$$

where h_{ref} is the reference enthalpy, T_{ref} is the reference temperature, and c_p is the specific heat at constant pressure.

Table 3 Case studies

Case	Material	Insert	Metal/ module (kg)	PCM/ module (kg)	Total LHTESS (tons)
1	Steel	Plate	~370	515	7.1
2	Al	Plate	~126	515	5.1
3	Al	Perforated	~38	580	4.3
4	Al 8 mm	Perforated	~48	572	4.3

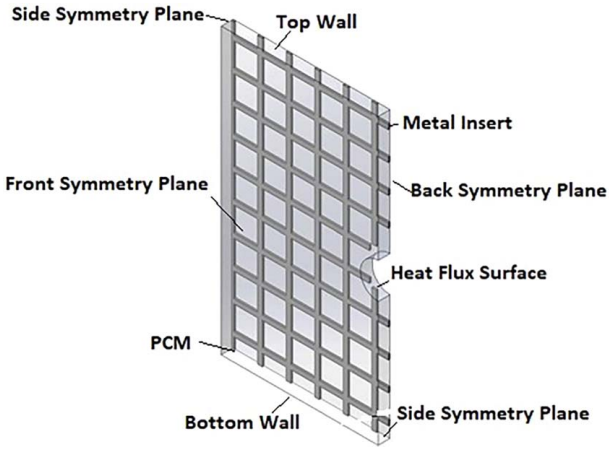

Fig. 5 LHTESS cell unit

The liquid fraction, β, can be defined as

$$\beta = 0 \quad \text{if } T < T_{\text{solidus}}$$
$$\beta = 1 \quad \text{if } T > T_{\text{liquidus}}$$
$$\beta = \frac{T - T_{\text{solidus}}}{T_{\text{liquidus}} - T_{\text{solidus}}} \quad \text{if } T_{\text{solidus}} < T < T_{\text{liquidus}}$$

The latent heat content can be presented in terms of the latent heat of the material, L

$$\Delta H = \beta L \tag{3}$$

The latent heat content can vary between zero (for a solid) and 1 (for a liquid).

For solidification/melting problems, the energy equation is written as

$$\frac{\partial}{\partial t}(\rho H) + \nabla(\rho v H) = +\nabla(k\nabla T) + S \tag{4}$$

where H is the enthalpy (defined in Eq. (1)), ρ is the density, v is the fluid velocity, and S is the source term.

The Fluent's power law differentiating scheme and a SIMPLE method for pressure–velocity coupling are used to solve the momentum and energy conservation equations. The PRESTO scheme is adopted for the pressure correction equation. In the present study, the time step was set to 0.25 s and the computational region is approximated with the mesh containing 100,000 elements. In the modeling of the cell unit of LHTESS, the mesh size and time step sensitivity analyses were performed. The desired computational mesh quality and magnitude of the time step were selected by gradual refinement of the mesh and reduction of the time step until nor further significant improvements in results was detected.

The assumptions made in the proposed model are as follows:

- The properties of the PCM are considered to be constant in both the solid and the liquid phases. Thermophysical properties of PCM used in the modeling procedure are listed in Table 2.
- The natural convection effects are modeled using the Boussinesq approximation.
- The effect of the thermal expansion is disregarded.
- The constant and uniform heat flux on the surface of heat pipes was calculated, considering that the heat transfer capacity for each heat pipe is 100 W.
- Thermal contact resistances are ignored at all interfaces. There is no thermal bonding between the metallic inserts in the PCM and heat pipes, and a gap of 0.5 mm between these two elements is used in simulations.
- In the LHTESS cell unit, all vertical walls are symmetry planes and the upper and bottom boundaries are considered as adiabatic walls (see Fig. 5).

4.1 Numerical Results for the Latent Heat Thermal Storage System Discharging Process. The initial temperature for modeling the discharging process was assumed to be 230 °C. At this temperature, the PCM is in the liquid phase at the start of simulations. The uniform heat flux of 6200 W/m^2 is defined on the heat pipes external surface (see Fig. 5).

The variation in the PCM liquid volume fraction is shown in Fig. 6 for the discharging (solidification) process. It can be observed that the solidification starts immediately in all three cases and the solidification rate is constant throughout the process. For case 1 (steel plate), the solidification rate decreases after the instance, when there is 5% of the liquid fraction left in the PCM. Table 4 summarizes information from numerical results on the discharging time. It can be observed that there is no significant difference in the discharging times, and in all four cases, the required thermal energy is provided during the 4-h period for the ORC operation. Therefore, the discharging process depends mainly on the thermal managing capacity of the heat pipes.

The average temperature of the PCM for the discharging/solidification process is shown in Fig. 7. It can be observed that the temperature decreases linearly during the solidification for cases in which the aluminum metallic inserts are used. However, the average temperature of the PCM for case 1 decreases significantly after first 3 h in the process.

The final average temperature of the PCM after the discharging process for case 1, in which steel metallic inserts are used, is almost 10 °C lower than the solidus temperature, which means that afterwards LHTESS would require longer charging time.

The liquid fraction contours after the 3 h of discharging process are shown in Fig. 8. The solidification process is mainly predefined by the conduction phenomena, but there is a small temperature stratification due to the natural convection. It is important to highlight that the heat transfer process dynamics changes across the whole

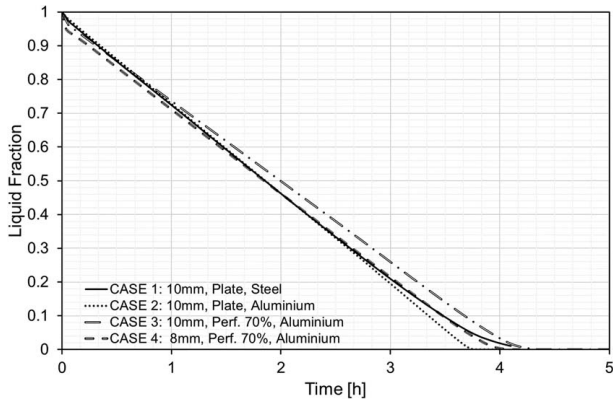

Fig. 6 Variation of the liquid fraction as a function of time during the discharging process

Table 4 Numerical results for modeling the discharging process

Case	Discharging time (h)	PCM T_{avg} solidification (°C)	Discharging time for 70% PCM (h)
1	4.2	209	2.6
2	3.8	217	2.6
3	4.4	212	2.8
4	4.1	213	2.7

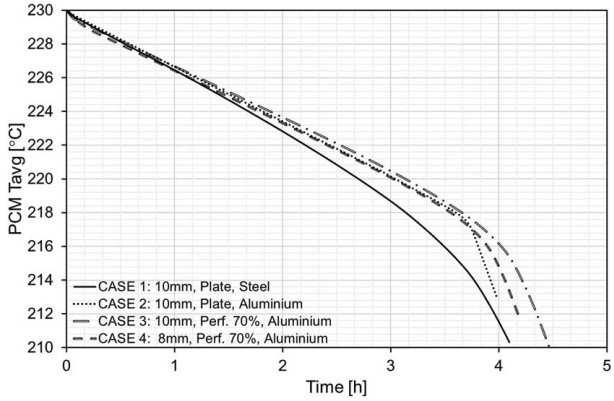

Fig. 7 Variation in the PCM average temperature during the discharging process

LHTESS because of the interaction of heat transfer phenomena in neighboring LHTESS cell units, especially in the vertical direction.

4.2 Numerical Results for the Latent Heat Thermal Storage System Charging Process. During the charging process, two initial constant temperatures were used, namely, 218 and 210 °C. In both cases, all PCMs initially are in the solid phase. The charging process is modeled by setting a constant and uniform heat flux of 6200 W/m^2 along the heat pipes external surface (see Fig. 5), corresponding to the heat pipe heat transfer capacity of 100 W.

The variation in the PCM liquid volume fraction for the charging (melting) process from the initial solidus temperature is shown in Fig. 9. It can be seen that for the situation, in which the initial temperature is 218 °C, the melting starts immediately in all three cases.

In case 1 (steel plate), the melting rate decreases significantly after 70% of the liquid fraction is achieved and the most likely reason of such behavior is due to the natural convection process being weakened, as it can be observed in Fig. 10 for the instance when the 2.5 h period is elapsed.

In case of the full-scale LHTESS module, it is expected that the charging time will be shorter due to the interaction of cell units mainly in the vertical direction (affected by free convection flows).

The average temperature of the PCM during the charging process is shown in Fig. 11. It is observed that the average temperature is practically the same for all cases during the first hours.

Figure 12 shows temperature contours for the instances when 2.5 h are elapsed for cases studied. During this period, the average temperature is the same but the temperature gradient in the PCM is higher for case with a steel plate (see Fig. 12).

Table 5 summarizes the numerical results on charging time for the LHTESS cell unit with the initial temperature of 218 °C. It can be observed that for the aluminum plates, the charging process is approximately 40 min shorter compared to cases with steel fins. The charging rate is practically the same in both cases until 70% of the liquid fraction is formed.

Comparing the charging and discharging results, it can be concluded that the charging time is not less than the discharging period and these are due to the boundary conditions deployed in the numerical model, including the constant heat flux applied. If numerical modeling of the whole LHTESS is conducted, then it is anticipated that the melting process starting at the solidus temperature takes less time than solidification [22].

In the numerical evaluation of the discharging time, it was observed that the average temperature of the PCM after the solidification is below 210 °C for case 1. Considering this, the charging process was modeled starting at the initial temperature of 210 °C. The variation in the PCM liquid volume fraction for such situations is shown in Fig. 13. It can be observed that prior to the melting process, there is an initial stage of heating up metallic inserts;

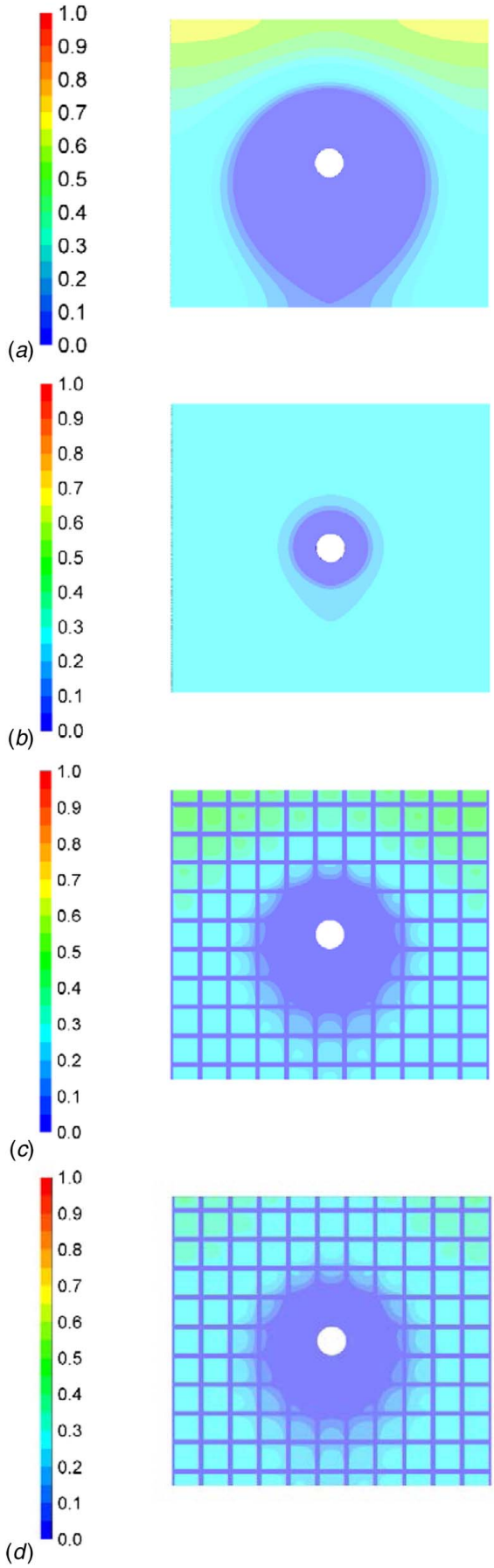

Fig. 8 Contours of PCM liquid fraction during discharging at 3 h: (*a*) case 1, (*b*) case 2, (*c*) case 3, and (*d*) case 4

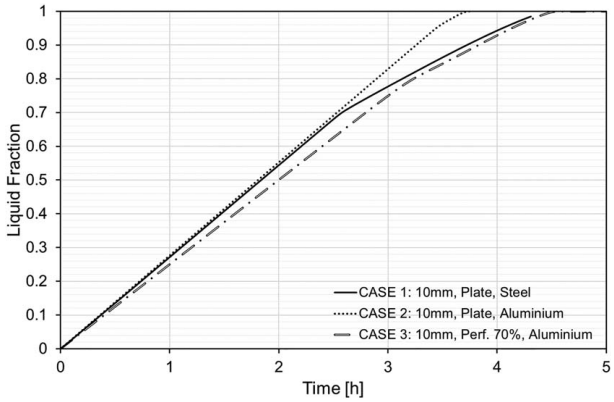

Fig. 9 Liquid fraction during the charging process ($T_i = 218$ °C)

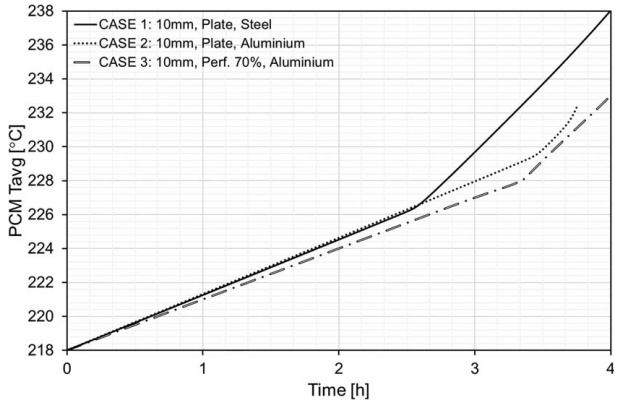

Fig. 11 PCM average temperature during the charging process ($T_i = 218$ °C)

therefore, at this stage, the aluminum inserts provide more rapid rise in the PCM average temperature, but the speed of the melting process is slower than in case 1 (Fig. 14). For case 1 (steel plate), it is also observed that the melting rate significantly decreases after 70% of the liquid fraction is formed.

Table 6 summarizes information on the charging time for these initial conditions. The charging time for 70% of PCM being melted increases by approximately 30 min in all cases compared to results presented in Table 5.

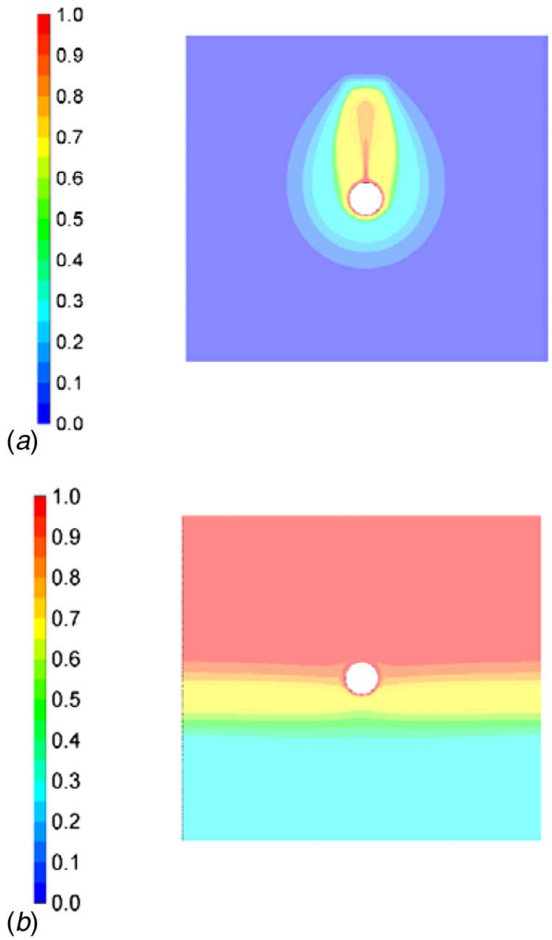

Fig. 10 Contour of PCM liquid fraction during the charging process from the 218 °C level. Case 1: (*a*) 0.5 h period is elapsed and (*b*) 2.5 h period is elapsed.

The numerical results indicate the similar performance for all three cases in terms of discharging and charging times. The main difference between these cases is the final average temperature and the temperature gradient in the PCM as it can be observed in Fig. 15.

It is important to note that there is a temperature stratification across the whole LHTESS after the charging process is completed due to induced natural convection flows inside the storage. The influence of such temperature stratification on the performance of the LHTESS should be evaluated in further studies.

5 Experimental Validation

The numerical model in this current work is identical to that deployed in Ref. [27]. The numerical model in Ref. [27] was calibrated using the corresponding experimental setup shown in Fig. 16. Comparison of numerical and experimental results in Ref. [27] shows a good agreement, demonstrating the validity of the selected numerical approach. Additionally, experimental setup in Ref. [27] is similar to cases 1 and 2, numerically simulated in this work. Therefore, comparison of two sets of data in Ref. [27] indicates the correctness of the numerical model used in this study.

The following is the detailed description of the numerical model calibration procedure used in Ref. [27].

First, six K-type thermocouples were placed inside each internally finned container to register the PCM temperature during the melting and solidification processes. All the thermocouples were placed between two central fins at certain locations. Then, the container was filled with the PCM and heating cartridge was placed inside the wooden box and connected to the power source. The PCM temperatures at the monitoring points were recorded every minute using a Picolog data logger. All experiments were carried out at the ambient temperature of 20 °C and repeated twice.

The ideal initial condition for the experiments would be the uniform PCM's temperature close to the melting point. For that reason, all the experiments were commenced with supplying the maximum power to reach the temperature level greater than 215 °C in all monitoring points, followed by a cool down period until the temperatures are close to 210 °C. Once this condition is reached, the power of the cartridge was set to a certain level. After completing the melting process, the power supply is switched off to monitor the solidification process. For comparison and validation purposes, the power input of 35 W was used for both prototypes.

The accuracy of used thermocouples is ±2.5 °C (1.2%) in the temperature range during the experiment. Their response time is 0.8 s. The accuracy of the PICO USB TC-08 thermocouple data logger is ±0.025 °C with the maximum frequency of sampling equal to 10 Hz. The lowest temperature measured in the present study is 210 °C. The overall uncertainty from the use of a

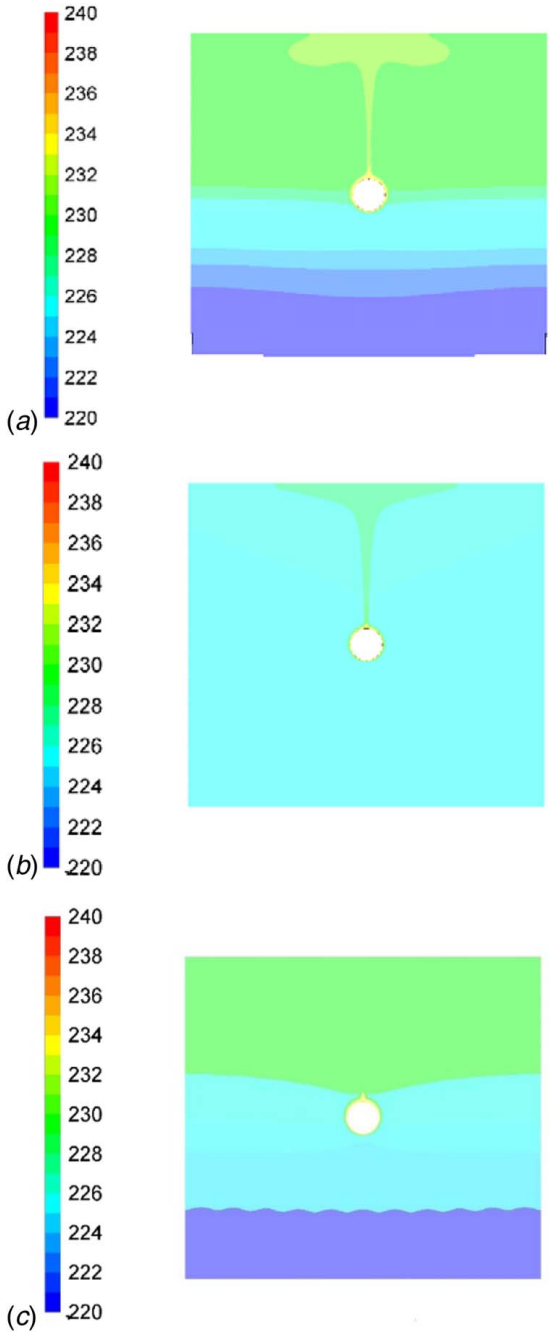

Fig. 12 PCM temperature contours during the charging process starting at the 218 °C level at 2.5 h: (*a*) case 1, (*b*) case 2, and (*c*) case 3

Table 5 Numerical results for the charging process ($T_i = 218$ °C)

Case	Charging time (h)	PCM T_{avg} after melting (°C)	Charging time for 70% PCM (h)
1	4.5	242	2.6
2	3.8	232	2.5
3	4.5	238	2.8

temperature measuring system is 1.2%. The error in positioning of thermocouples is about ±2 mm. The heater is powered by an AC power supply unit, providing an accuracy of ±3%. The total magnitude of uncertainty in the determination of experimental results does not exceed 8%.

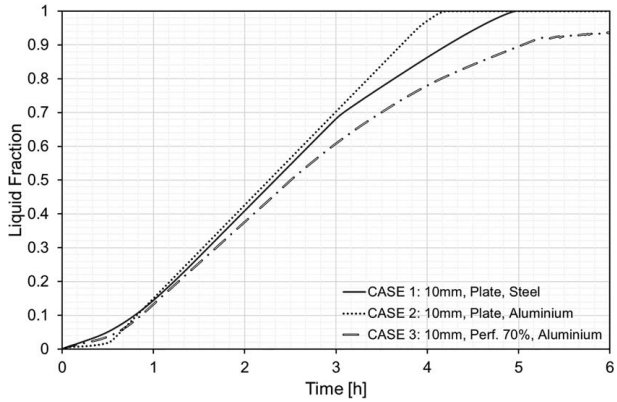

Fig. 13 Liquid fraction during the charging process ($T_i = 210$ °C)

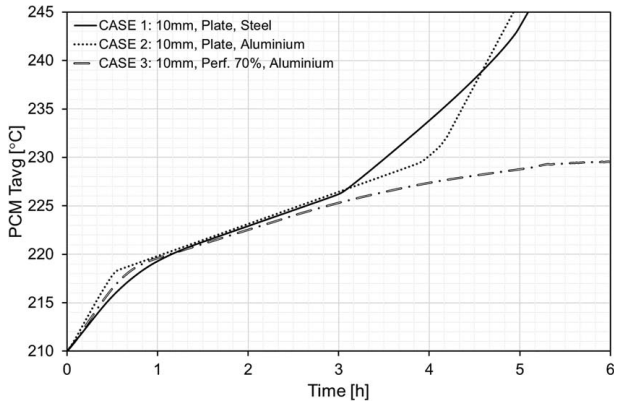

Fig. 14 PCM average temperature during the charging process ($T_i = 210$ °C)

Table 6 Numerical results for the charging process ($T_i = 210$ °C)

Case	Charging time (h)	PCM T_{avg} after melting (°C)	Charging time for 70% of PCM being melted (h)
1	5.0	243	3.1
2	4.2	232	3.0
3	>6.2	~230	3.5

Table 7 shows the experimental and numerical results for the melting and solidification times in both containers studied [27]. Numerical information on the formed liquid fraction is also presented for corresponding elapsed times. It can be observed that for the melting process, numerical and experimental results agree well with the accuracy within 7%. However, the numerical and experimental results for solidification processes deviate by 18%. The main reason for such a difference is that the solidification process is a free cooling process, occurring over a night period, and the rate of heat extraction is not fully controlled.

The temperature changes during the charging/melting process, obtained experimentally and numerically for the aluminum prototype, are shown in Fig. 17. Figure 17(*a*) shows experimental results, and Fig. 17(*b*) presents numerical results on the liquid fraction formation obtained during the melting process. The experimental temperature curves (see Fig. 17(*a*)) rise gradually at the initial stage, but the phase change process, as it can be seen, occurs at close values of temperatures. It can be seen in Fig. 17(*b*) that the phase change process starts at 218.9 °C and finishes at 225.0 °C.

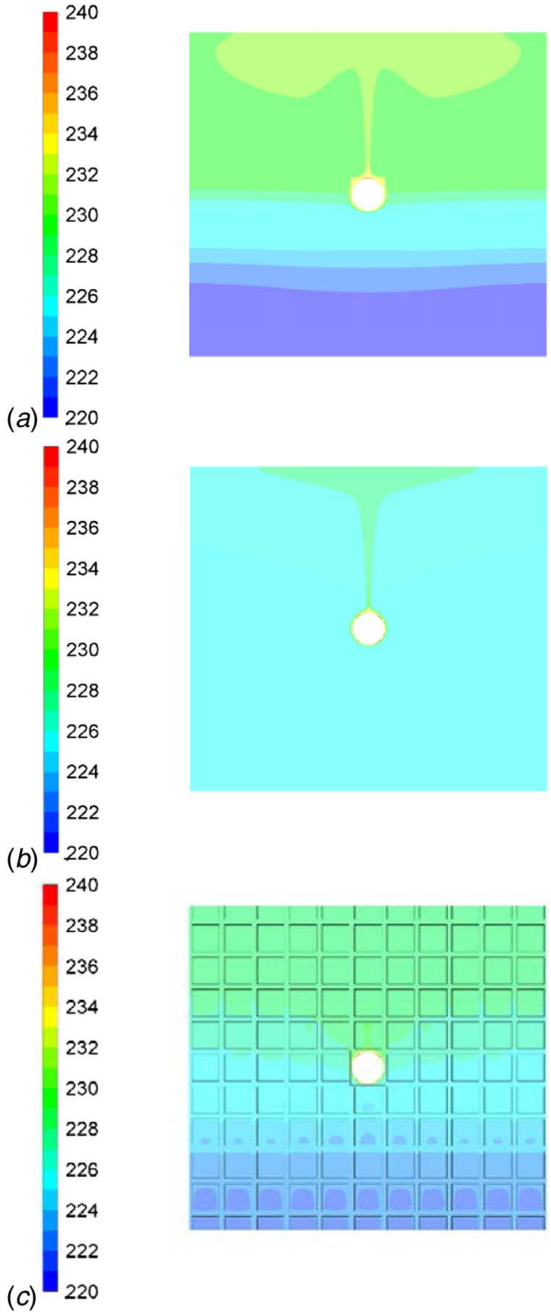

Fig. 15 PCM temperature contours during the charging process starting from the 210 °C level at 3 h: (*a*) case 1, (*b*) case 2, and (*c*) case 3

Fig. 16 Top view of the container with the PCM [27]

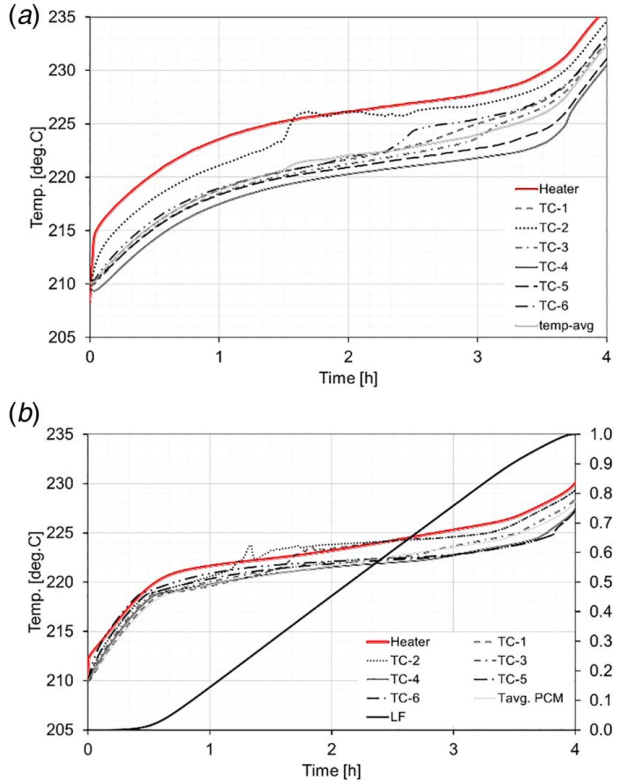

Fig. 17 Temperature variations during the melting process in the aluminum container: (*a*) experimental and (*b*) numerical results [27]

Table 7 Experimental and numerical results [27]

	Melting TC-4 = 225 °C	Solidification TC-4 = 212 °C
Steel experimental	4.7 h	4.2 h
Steel numerical	4.4 h (LF = 82%)	4.5 h (LF = 11%)
Al experimental	3.7 h	4.0 h
Al numerical	3.8 h (LF = 97%)	4.8 h (LF = 0%)

6 Conclusions

The preliminary evaluation of the LHTESS performance allows us to draw the following conclusions:

- All three configurations of the LHTESS with metal inserts, used to enhance the heat transfer processes inside the LHTESS, provide the required thermal energy discharging rate.
- In terms of charging or discharging times, there is no significant reduction when using aluminum inserts instead of steel fins.
- The main advantage in using aluminum inserts is the more uniform average temperature and smaller temperature gradient in the LHTESS. The charging process of the LHTESS using aluminum inserts is shorter in time because the initial temperature is closer to the phase change temperature.
- The simplified numerical model used in this study does not predict the anticipated reduction in charging time compared to the discharging process. The reason is the selected small dimensions of the used LHTESS cell unit, which suppresses the effect of the natural convection flows at the final stage of the melting process. Therefore, in future investigations, it is necessary to use the model, which is based on the simulation of cell unit, which has the vertical dimension equal to the

height of the LHTESS module and includes a corresponding full set of heat pipes.
- The work is in progress on the development of a numerical model for the complete single module of LHTESS, and computational results will be validated using experimental data from testing such a full-scale module.
- The absence of the thermal bonding between fins and heat pipes does not result in a significant reduction of charging or discharging periods in cases in which aluminum fins are used. Another advantage from using aluminum fins is that there is a lower temperature gradient across the LHTESS.

Acknowledgment

This study was supported with funding from the European Union's Horizon 2020 Research and Innovation Actions Programme (Project Grant Agreement No. 723596; Funder ID: 10.13039/501100007601) (INNOVA MICROSOLAR) and Marie Sklodowska-Curie Actions (Grant Agreement No. 705944; Funder ID: 10.13039/100010665) (THERMOSTALL).

Nomenclature

H = enthalpy (J/kg)
S = source term (J/m^3 s)
c_p = specific heat at constant pressure (J/kg K)
c_{pl} = specific heat in the liquid state (J/kg K)
c_{ps} = specific heat in the solid state (J/kg K)
h_{ref} = reference enthalpy (J/g)
k_l = thermal conductivity in the liquid state (W/m K)
H_m = heat of fusion (J/kg)
H_s = heat of solidification (J/kg)
T_m = melting temperature (°C)
T_{ref} = reference temperature (°C)
T_s = solidification temperature (°C)
β = liquid fraction (–)
μ_l = dynamic viscosity (cP)
v = fluid velocity (m/s)
ρ_l = density in liquid state (kg/m^3)

References

[1] Sasaguchi, K., and Viskanta, R., 1989, "Phase Change Heat Transfer During Melting and Resolidification of Melt Around Cylindrical Heat Source(s)/Sink(s)," ASME J. Energy Resour. Technol., **111**(1), pp. 43–49.
[2] Aceves-Saborio, S., Nakamura, H., and Reistad, G. M., 1994, "Optimum Efficiencies and Phase Change Temperatures in Latent Heat Storage Systems," ASME J. Energy Resour. Technol., **116**(1), pp. 79–86.
[3] Pinelli, M., and Piva, S., 2003, "Solid/Liquid Phase Change in Presence of Natural Convection: A Thermal Energy Storage Case Study," ASME J. Energy Resour. Technol., **125**(3), pp. 190–198.
[4] Archibold, A. R., Bhardwaj, A., Rahman, M. M., Goswami, D. Y., and Stefanakos, E. L., 2016, "Comparison of Numerical and Experimental Assessment of a Latent Heat Energy Storage Module for a High-Temperature Phase-Change Material," ASME J. Energy Resour. Technol., **138**(5), p. 052007.
[5] Studniorz, A., Wolf, D., Christidis, A., and Tsatsaronis, G., 2018, "Active Phase Change Material Cold Storage in Off-Grid Telecommunication Base Stations: Potential Assessment of Primary Energy Savings," ASME J. Energy Resour. Technol., **140**(11), p. 112007.
[6] Nnaemeka, O. J., and Bibeau, E. L., 2019, "Application of Low-Temperature Phase Change Materials to Enable the Cold Weather Operability of B100 Biodiesel in Diesel Trucks," ASME J. Energy Resour. Technol., **141**(6), p. 062008.
[7] Zhai, W., Yang, B., Li, M., Li, S., Xin, M., Lin, J., and Wang, L., 2015, "Preparation of Multi Nitrate Molten Salt and Its Properties Tests," 2015 International Symposium on Material, Energy and Environment Engineering, Changsha, China, Nov. 28–29.
[8] Kenisarin, M. M., 2010, "High-Temperature Phase Change Materials for Thermal Energy Storage," Renew. Sustain. Energy Rev., **14**(3), pp. 955–970.
[9] Solé, A., Neumann, H., Niedermaier, S., Martorell, I., Schossig, P., and Cabeza, L. F., 2014, "Stability of Sugar Alcohols as PCM for Thermal Energy Storage," Sol. Energy Mater. Sol. Cells, **126**, pp. 25–134.
[10] Bauer, T., Breidenbach, N., Pfleger, N., Laing, D., and Eckand, M., 2012, "Overview of Molten Salt Storage Systems and Material Development for Solar Thermal Power Plants," Proceedings of the 2012 National Solar Conference for (SOLAR 2012), Denver, CO, May 13–17, pp. 1–8.
[11] Bauer, T., Pfleger, N., Breidenbach, N., Eck, M., Laing, D., and Kaesche, S., 2013, "Material Aspects of Solar Salt for Sensible Heat Storage," Appl. Energy, **111**, pp. 1114–1119.
[12] Costa, S. C., Mahkamov, K., Kenisarin, M., Lynn, K., Halimic, E., and Mullen, D., 2018, "Solar Salt Latent Heat Thermal Storage for a Small Solar Organic Rankine Cycle Plant," ASME 2018 12th International Conference on Energy Sustainability Collocated with the ASME 2018 Power Conference and the ASME 2018 Nuclear Forum, p. V001T08A002, ASME Paper No. ES2018-7326.
[13] Martin, C., Bauer, T., and Müller-Steinhagen, H., 2013, "An Experimental Study of a Non-Eutectic Mixture of KNO_3 and $NaNO_3$ With a Melting Range for Thermal Energy Storage," Appl. Therm. Eng., **56**(1–2), pp. 59–166.
[14] Gaona, D., Urresta, E., Marínez, J., and Guerrón, G., 2017, "Medium-Temperature Phase-Change Materials Thermal Characterization by the T-History Method and Differential Scanning Calorimetry," Exp. Heat Transfer, **30**(5), pp. 463–474.
[15] Iverson, B. D., Broome, S. T., Kruizenga, A. M., and Cordaro, J. G., 2012, "Thermal and Mechanical Properties of Nitrate Thermal Storage Salts in the Solid-Phase," Sol. Energy, **86**(10), pp. 2897–2911.
[16] Pacheco, J. E., Ralph, M. E., Chavez, J. M., Dunkin, S. R., Rush, E. E., Ghanbari, C. M., and Matthews, M. W., 1995, "Results of Molten Salt Panel and Component Experiments for Solar Central Receivers: Cold Fill, Freeze/Thaw, Thermal Cycling and Shock, and Instrumentation Tests," No. SAND-94-2525, Sandia National Labs, Albuquerque, NM.
[17] Fawsitt, C. E., 1908, "Viscosity Determinations at High Temperatures," J. Chem. Soc. Trans., **93**, pp. 1299–1307.
[18] Jin, Y., Cheng, J., An, X., Su, T., Zhang, P., and Li, Z., 2016, "Accurate Viscosity Measurement of Nitrates/Nitrites Salts for Concentrated Solar Power," Sol. Energy, **137**, pp. 385–392.
[19] Mahkamov, K., Pili, P., Manca, R., Leroux, A., Mintsa, A. C., Lynn, K., and Costa, S. C., 2018, "Development of a Small Solar Thermal Power Plant for Heat and Power Supply to Domestic and Small Business Buildings," ASME 2018 12th International Conference on Energy Sustainability Collocated With the ASME 2018 Power Conference and the ASME 2018 Nuclear Forum, p. V001T06A014, ASME Paper No. POWER2018-7336.
[20] Zhao, J., Rao, Z., Liu, C., and Li, Y., 2016, "Experimental Investigation on Thermal Performance of Phase Change Material Coupled With Closed-Loop Oscillating Heat Pipe (PCM/CLOHP) Used in Thermal Management," Appl. Therm. Eng., **93**, pp. 90–100.
[21] Chen, J., Yang, D., Jiang, J., Ma, A., and Song, D., 2014, "Research Progress of Phase Change Materials (PCMs) Embedded With Metal Foam (A Review)," Procedia Mater. Sci., **4**, pp. 389–394.
[22] Tiari, S., Qiu, S., and Mahdavi, M., 2015, "Numerical Study of Finned Heat Pipe-Assisted Thermal Energy Storage System With High Temperature Phase Change Material," Energy Convers. Manage., **89**, pp. 833–842.
[23] Lohrasbi, S., Miry, S. Z., Gorji-Bandpy, M., and Ganji, D. D., 2017, "Performance Enhancement of Finned Heat Pipe Assisted Latent Heat Thermal Energy Storage System in the Presence of Nano-Enhanced H_2O as Phase Change Material," Int. J. Hydrogen Energy, **42**(10), pp. 6526–6546.
[24] Tiari, S., Qiu, S., and Mahdavi, M., 2016, "Discharging Process of a Finned Heat Pipe-Assisted Thermal Energy Storage System With High Temperature Phase Change Material," Energy Convers. Manage., **118**, pp. 426–437.
[25] Guo, C., and Zhang, W., 2008, "Numerical Simulation and Parametric Study on New Type of High Temperature Latent Heat Thermal Energy Storage System," Energy Convers. Manage., **49**(5), pp. 919–927.
[26] Ansys, Inc, 2017, ANSYS FLUENT 18.2 Theory Guide.
[27] Costa, S. C., Mahkamov, K., Kenisarin, M., Ismail, M., Halimic, E., Mullen, D., and Werner, T., 2018, "Experimental and Numerical Study on Melting of Solar Salt in a Finned Metallic Container," ASME 2018 International Mechanical Engineering Congress and Exposition, p. V06BT08A055, ASME Paper No. IMECE2018-88072.